JOURNAL OF AIRCRAFT
Vol. 47, No. 4, July–August 2010

# Pitch and Heave Control of Robotic Samara Micro Air Vehicles

Evan R. Ulrich,[*] J. Sean Humbert,[*] and Darryll J. Pines[†]
*University of Maryland, College Park, Maryland 20742*

DOI: 10.2514/1.47197

**Micro/nano unmanned aerial systems are an emerging class of vehicles uniquely suited to performing covert missions. A linear model for the heave dynamics of a robotic samara (winged seed) in hovering flight was identified from data collected external to the vehicle by a visual tracking system. Insight gleaned from the implementation of feedback control includes a characteristically overdamped system in climb, which differs from the underdamped descent characteristic observed. Identification and error estimation efforts used a frequency response-based system identification. The two robotic samara vehicles of differing scale compared in this study represent the first demonstration of controlled flight of a vehicle of this kind.**

## Nomenclature

$A$ = dynamics matrix
$B$ = control matrix
$C$ = output matrix
$dy$ = differential element
$F_{\mathrm{CF}}$ = centrifugal force
$F_G$ = gravity force
$F_P$ = propulsive force
$F_{W_D}$ = drag force
$F_{W_L}$ = lift force
$G_p(s)$ = plant transfer function
$I_x, I_y, I_z$ = principal moments of inertia
$K$ = static gain
$K(s)$ = controller
$K_d$ = derivative gain
$K_i$ = integral gain
$K_p$ = proportional gain
$p, q, r$ = rotational velocities
$R_{BF}$ = transforms fixed frame **F** to body frame **B**
$R_{xx}$ = input autospectral density
$R_{xy}$ = input/output cross-spectral density
$R_{yy}$ = output autospectral density
$T_{pl}$ = time constant
$u, v, w$ = translational velocities
$W(s)$ = heave transfer function
$\dot{w}$ = heave acceleration
$X$ = state vector
$x, y, z$ = inertial frame position
$Y$ = control output
$Y_d$ = reference value
$Z_w$ = heave stability derivative
$Z_{\theta_0}$ = collective pitch stability derivative
$\beta$ = coning angle
$\epsilon_i$ = infinitesimal quantity
$\Theta(s)$ = collective pitch transfer function
$\theta_0 \in [-1, 1]$ = control input
$\phi, \theta, \psi$ = Euler angles

## I. Introduction

IN RECENT years, a new paradigm of flight has emerged that encompasses microscale aircraft that are bioinspired. These highly maneuverable platforms are capable of hovering flight and are ideally suited for operation in a confined environment. The reconnaissance mission envisioned requires a high level of autonomy due to the fast dynamics of the vehicle and the limit on communication in the likely areas of operation (i.e., caves and buildings). Development of a state-space model of the system dynamics about a trimmed flight condition will facilitate future model-based controller and observer design, enabling autonomous operation.

Aerial systems that satisfy the dimensional constraints outlined by the Defense Advanced Research Projects Agency (DARPA) micro air vehicle (MAV) initiative include fixed-wing, rotary-wing, and flapping-wing vehicles. The simplest and most mature of these platforms are fixed-wing vehicles that boast speed, simplicity, and well-known dynamics; however, the limitation imposed by forward flight restricts functionality in cluttered environments, which can be traversed by rotary- and flapping-wing platforms. Microscale helicopter linear dynamic system models have been described by Conroy et al. [1], using system identification tools developed by Tischler and Remple [2] and Mettler et al. [3] for substantially larger vehicles, including the Yamaha RMAX helicopter. Despite the growing interest in microscale helicopter flight, a dynamic model of a single-winged rotorcraft has not been developed.

A substantial challenge in modeling the dynamics of microscale flight is the general lack of knowledge of the complex low-Reynolds-number flow regime they inhabit. Additionally, the vehicles are highly susceptible to wind gusts as a result of low vehicle inertia. The complexity of the system can be reduced substantially by identifying a linear model that describes its reaction to forces imposed by a control input. A model description of this nature lends itself well to modern control and state estimation.

The intent of this manuscript is to characterize the flight dynamics and control of a rotary-wing MAV based on one of nature's most efficient fliers: the seed of the maple (acer) tree, or the samara. Identification and error estimation of the vehicle dynamic model was done with data collected by a visual tracking system[‡] and usation of a frequency response-based system identification package developed at the U.S. Army Aeroflightdynamics Directorate located at Moffett Field, California. Frequency-domain system identification is limited to linear models, valid only for small perturbations about the trimmed condition.

Model structure is based on a reduction of the longitudinal dynamics of a helicopter in hover to a linear system described by stability derivatives. Cramer–Rao (CR) insensitivity bounds describe

---

Received 15 September 2009; revision received 22 January 2010; accepted for publication 15 March 2010.

[*] Department of Aerospace Engineering.

[†] Dean of Engineering.

[‡] Data available online at http://www.vicon.com/_pdfs/t_cameras.pdf [retrieved 22 May 2008].

the likely error resulting from multiple trials and are used to validate the estimates of the identified parameters. Additional validation of the linear model is done through implementation of a linear controller, with feedback provided by the visual tracking system.

## II. Vehicle Description

The concept of a single-wing rotating aircraft is not a new one and, in fact, the first vehicle of this type was flown in 1952, in the woods surrounding Lake Placid, New York, by Charles W. McCutchen [4]. A more recent vehicle was developed and flown by a team led by Lockheed Martin Advanced Technology Laboratories [5]. The prototype, called MAVPro, incorporated an outrunner motor with an 8-in.-diam propeller; it weighed 0.514 kg, rotated at a stable 4 Hz, and could climb to 50 ft with radio-controlled actuation of a trailing-edge flap. The MAVPro incorporated the AG38 airfoil and exhibited a rectangular planform geometry. The various single-winged rotating aircraft developed over the years have made no attempt to use the most basic mode of transit of the natural samara: autorotation. Additionally, airfoil cross sections and planform designs have had no similarity to those found in natural samaras.

The authors intent in the design of the vehicles discussed herein was to emulate the natural samara and, in doing so, take advantage of the highly efficient autorotation it employs. As such, samaras I and II use unconventional and samara-inspired planform geometry and airfoil cross sections developed previously by Ulrich and Pines [6,7]. These vehicles perform stable autorotation and are capable of landing at terminal velocity without sustaining any damage. In the event of motor failure, the vehicles gently autorotate back to the ground.

Conventional monocopter designs apply torque to the vehicle with a thrust device slightly offset from the $\hat{c}_y$ axis and, in the case of MAVPro, the propeller spins in the $\hat{c}_y$-$\hat{c}_z$ plane and influences the stability about the $\hat{c}_y$ axis. This configuration results in the propeller fighting the pitch input from the flap and reduces controllability of the vehicle. The 3.5-in.-diam propellers of samaras I and II are spinning in the $\hat{c}_x$-$\hat{c}_z$ plane and oppose applied torque about the $\hat{c}_x$ axis, providing additional roll stability. The configurations of samaras I and II permit control of rotation rate, altitude, and translation via the appropriate actuation of the wing servo. The component layout and free-body diagram of the vehicle used in this study are shown in Fig. 1. The sign convention and corresponding vehicle orientation are shown in Fig. 2.

The design and construction of the samaras used in these experiments was done with the intent of providing a stable vehicle that could be tested in a limited area. The unconventional wing and body structure are the result of an iterative design process that has produced on the order of 100 vehicles. The resultant vehicles are extremely damage tolerant as they employ flexible structures that deflect upon impact, effectively increasing the time over which the impact load is applied to the vehicle. The configuration and dimensions of the vehicles are shown in Figs. 2 and 3. Advantages over traditional microscaled vertical takeoff and landing configurations include passive stability, efficient autorotation, low body drag, mechanical simplicity, low cost, high payload capacity, and substantial damage tolerance.

## III. Vehicle Design

The primary load-bearing structure of the vehicle is 0/90-ply 0.025-thick carbon-fiber composite laminate, with opposed parallel tension and compression members mounted to the motor and wing. In this configuration, the structure provides a high degree of flexure in the $\hat{c}_z$ direction and a high degree of stiffness in the plane of rotation. The angle at which the motor is held provides protection from ground impingement on takeoff and landing.

The flight time of the samara I is roughly 20 min, with a 0.025 kg, 480 mAh, 7.4 V, and two-cell lithium–polymer (LiPo) battery, for a total vehicle mass [gross weight (GW)] of 0.075 kg. The maximum gross takeoff weight (GTOW) of the vehicle is 0.125 kg, and the maximum dimension is 0.27 m (Fig. 2). The second, and smaller, samara tested, called samara II, is designed and constructed in a similar fashion to samara I. However, the total mass is 0.038 kg, and

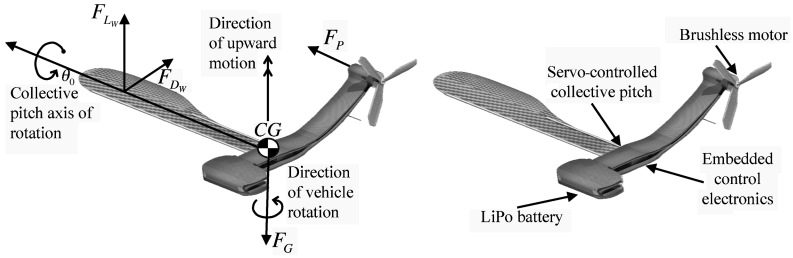

**Fig. 1 Robotic samara component and free-body diagram.**

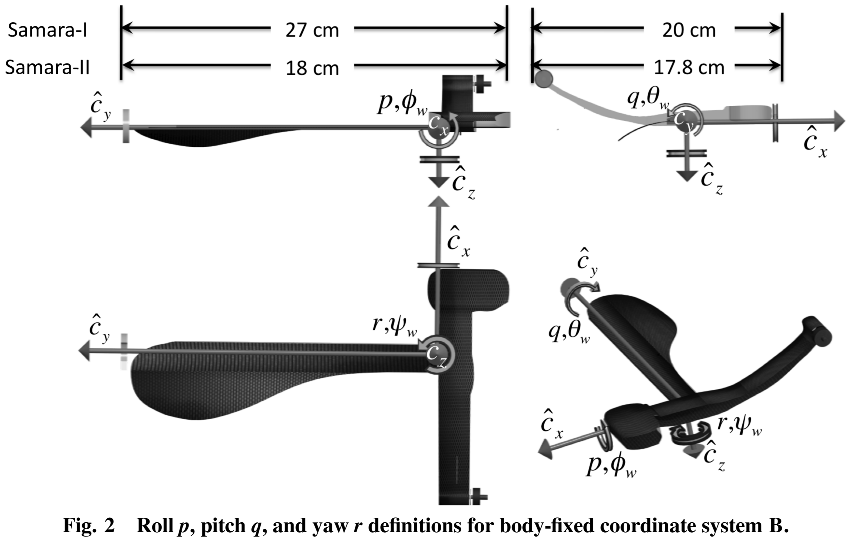

**Fig. 2 Roll $p$, pitch $q$, and yaw $r$ definitions for body-fixed coordinate system B.**

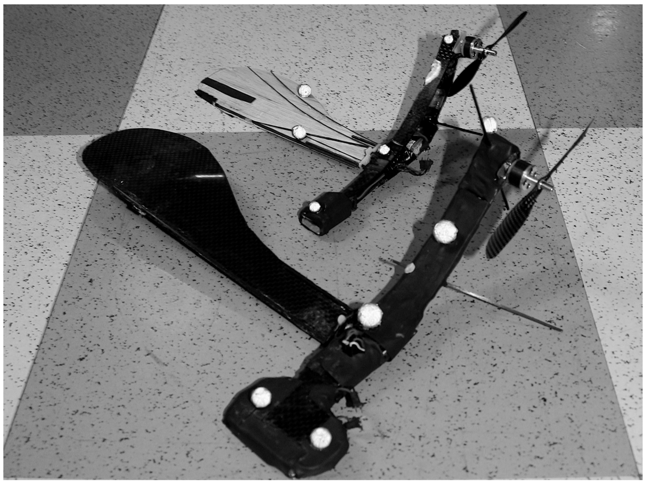

Fig. 3 Robotic samaras I and II in flight configuration.

the maximum dimension is 0.18 m (Fig. 2). Table 1 details the mass breakdown of samaras I and II, as well as two hobby radio-controlled rotorcraft. The mass breakdown is similar for the four vehicles; however, the samara benefits from a less complex, and therefore lighter, propeller/rotor system and requires no transmission, as it directly drives the propeller. This decrease in complexity creates a more robust and reliable system.

Pines and Bohorquez [8] found the propulsion systems of small-scale fliers typically exceed 60% of the total vehicle mass, compared with a jetliner that boasts a propulsion system with a 40% mass fraction. The 20% savings at full scale is used entirely for payload, as the Boeing 767 payload mass fraction is 29%, compared with 9% for small-scale flight vehicles. The mass fraction of the propulsion system of samaras I and II without payload is 47 and 42%, respectively. If we consider the vehicles' maximum GTOW for this calculation, the mass fractions of the propulsion system drop to 28 and 35%, respectively, with payload fractions of 40 and 21%.

## IV. Stability Properties

A substantial advantage of the samaras I and II vehicles is that it they are passively stable systems. A simple qualitative stability analysis of the samara I in a steady hover or autorotation illustrates this point. In a steady hover, the thrust from the propeller $F_P$ is balanced by the drag from the body and wing $F_{D_W}$, resulting in a near-constant rotational rate about its principal inertial axis $I_z$. The vertical force generated by the wing $F_{L_W}$ opposes the force of gravity $F_G$, resulting in a net zero vertical velocity. Alternatively, in autorotation, the resistive torque of the wing drag is equal to the driving torque of the lift, resulting in a net zero torque and vertical acceleration. Consider the assumed motion $r = r_0$ and $p, q \ll r_0$ in steady hover or autorotation. To investigate whether the motion is stable or not (neglecting aerodynamic contributions), a small moment is applied to the body, such that, after the moment is applied, the resultant angular velocities are as follows:

$$p = \epsilon_p \tag{1}$$

$$q = \epsilon_q \tag{2}$$

$$r = r_0 + \epsilon_r \tag{3}$$

where $\epsilon_i$ ($i = 1, 2, 3$) are infinitesimal quantities. To determine the evolution of these perturbed angular velocities in time, it is convenient to use the Euler equations as follows:

$$I_z(\dot{r}_0 + \dot{\epsilon}_r) + (I_x - I_y)\epsilon_p\epsilon_q = 0 \tag{4}$$

$$I_x\dot{\epsilon}_p - (I_y - I_z)(r_0 + \epsilon_r)\epsilon_q = 0 \tag{5}$$

$$I_y\dot{\epsilon}_q - (I_z - I_x)(r_0 + \epsilon_r)\epsilon_p = 0 \tag{6}$$

The change in angular velocities is small and, as such, allows linearization of the preceding equations by eliminating quadratic and higher-order terms in $\epsilon_i$, yielding

$$I_z\dot{\epsilon}_r = 0 \tag{7}$$

$$I_x\dot{\epsilon}_p - (I_y - I_z)r_0\epsilon_q = 0 \tag{8}$$

$$I_y\dot{\epsilon}_q - (I_z - I_x)r_0\epsilon_p = 0 \tag{9}$$

This implies $\epsilon_r$ is constant. The behavior of the remaining angular velocities can be understood with eigenvalue analysis. Assuming a solution of the form

$$\epsilon_p(t) = E_p e^{\lambda t} \tag{10}$$

$$\epsilon_q(t) = E_q e^{\lambda t} \tag{11}$$

Next, we can introduce the expansions into the linearized equations,

$$\begin{bmatrix} I_x\lambda & (I_z - I_y)r_0 \\ (I_x - I_z)r_0 & I_y\lambda \end{bmatrix}\begin{bmatrix} E_p \\ E_q \end{bmatrix} e^{\lambda t} = \begin{bmatrix} 0 \\ 0 \end{bmatrix} \tag{12}$$

The solution requires that the determinant of the coefficient matrix be zero, yielding the characteristic equation

$$I_x I_y \lambda^2 - (I_x - I_z)(I_z - I_y)r_0^2 = 0 \tag{13}$$

Table 1 Weight data (in terms of percent of GW)

| Parameter | Samara II | Samara I | Hobby rotorcraft 1 | Hobby rotorcraft 2 |
|---|---|---|---|---|
| Mass | 0.038 kg | 0.075 kg | 0.3 kg | 1.8 kg |
| Maximum GTOW | 0.048 kg | 0.125 kg | —— | —— |
| Maximum dimension | 0.18 m | 0.27 m | —— | —— |
| Percent GW | | | | |
| Propeller/rotor system | 5.3 | 2.6 | 11.0 | 11.2 |
| Tailboom assembly | 2.6 | 3.3 | 8.0 | 9.1 |
| Main motor (electric) | 10.5 | 10.7 | 15.4 | 10.5 |
| Fuselage/structure | 26.3 | 27.6 | 7.0 | 15.1 |
| Main transmission | Direct drive | Direct drive | 2.0 | 3.4 |
| Landing gear | 2.6 | 2.7 | 2.3 | 3.4 |
| Control system | 18.4 | 16.0 | 5.7 | 18.3 |
| Flight control avionics | 7.9 | 4.0 | 29.4 | 2.4 |
| Power source | 26.3 | 33.3 | 19.2 | 26.6 |
| Payload | 0 | 0 | 0 | 0 |
| Flight time | 10 min | 20 min | —— | —— |

**Table 2 Inertia properties, rotation rates, and resultant eigenvalues for robotic samaras I and II**

| | $I_x$, kg mm$^2$ | $I_y$, kg mm$^2$ | $I_z$, kg mm$^2$ | $r_0$, rad/s | $\lambda$, rad/s |
|---|---|---|---|---|---|
| Samara I | 248 | 562 | 797 | 80.5 | $\pm 0 + 77i$ |
| Samara II | 35 | 98 | 122 | 76 | $\pm 0 + 59i$ |

The solution is

$$\lambda = \pm i \sqrt{\frac{(I_x - I_z)(I_z - I_y) r_0^2}{I_x I_y}} \tag{14}$$

Two types of solutions are possible and depend on the principal moments of inertia. If $I_x > I_z$ and $I_y > I_z$, or if $I_x < I_z$ and $I_y < I_z$ (characteristic of samara I and samara II), both roots of the characteristic equation are imaginary. In the absence of nonconservative forces, the system is marginally stable [9]. The inertial parameters of the samara vehicles, as well as the resultant eigenvalues, are listed in Table 2.

## V. Experimental Setup

### A. Visual Tracking System

The position and orientation of each vehicle was collected at a rate of 500 Hz, using a Vicon visual tracking system. The system collects data by capturing two-dimensional (2-D) images of the subject, which is fitted with retroreflective markers. The Vicon system strobes light at the frame rate of the camera. The light incident on the surface of the marker returns to its source, reducing errors commonly caused by interference. The light returned to the lens allows for a quick computation of the centroid of the marker. The three-dimensional (3-D) position is obtained from a least-squares fit of the 2-D camera observations. The error in the system is determined by the calibration of the system, which is performed before any flight data can be taken. The noise observed in a given data set is consistent. During a flight test, the tracking system uses eight cameras to track the 3-D position of three retroreflective markers placed on the samara wing. Each marker is spherical, with a diameter of 5 mm. The 3-D shape of the marker allows for better tracking by the Vicon system. Figure 4 displays images of the virtual capture volume and the rigid body model of the samara wing created by the retroreflective markers.

### B. Telemetry Synchronization

Pitch input is measured by two methods, both onboard and offboard the vehicle. The state of the actuator is measured offboard the samara on an identical system receiving commands from the same transmitter. Two markers are placed on an arm attached to the offboard actuator to track the input to the vehicle. During a flight test, the samara vehicle and the offboard actuator are simultaneously tracked, allowing the angular displacement measured on the ground to be correlated to the motion of the samara vehicle, both of which are synchronized in time.

### C. Vehicle Inputs

It is advantageous to track the wing pitch angle via the offboard system, as it provides the ability to track the collective pitch inputs without the influence of the forces on the vehicle. The onboard method includes measuring both pitch angle $\theta$ and coning angle $\beta$ via the markers placed on the wing. It is interesting to compare the onboard and offboard measurements, as the onboard angles are influenced by the aerodynamic and centrifugal forces acting on the vehicle. The wing pitch angle $\theta_0$ of the vehicle in flight exhibits a once-per-revolution displacement. This variation results in a cyclical change in the coning angle $\beta$ and heave velocity not captured by the offboard measurements. In the absence of aerodynamic forces, the wing would assume an arbitrary orientation. However, in the presence of aerodynamic forces, a flapping moment is applied to the samara body, causing the wing to precess to a new orientation, restoring equilibrium to the system. Nothing was presumed to be known about what forces or deflection angles were generated, given a change in the actuator; therefore, all control inputs are normalized. The input command is given by $\theta_0$ for collective input and is normalized, such that $\theta_0 \in [-1, 1]$. The forces acting on the wing in flight, as well as the definition of the coning angle, are detailed in Fig. 5.

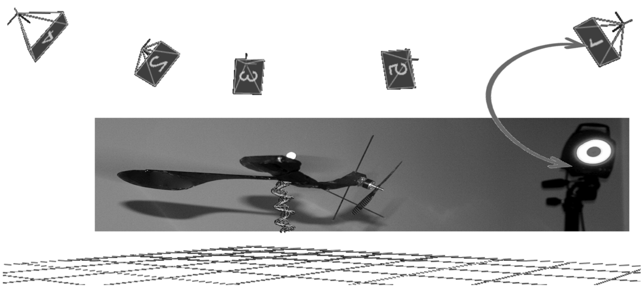

Fig. 4 Representative Vicon work space and flight path of samara II.

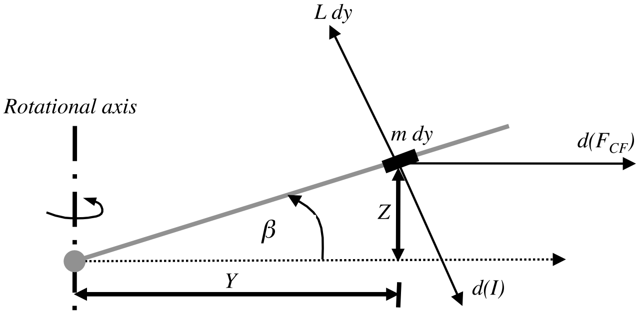

Fig. 5 Forces acting on element of a flapping robotic samara wing.

### D. Attitude Determination

The 3-D marker position data provide a means of resolving the orientation of the robotic samara in space. The three markers are sufficient to describe an orthonormal basis from which the rotation matrix representing the samaras orientation can be formed. The first vector forms the $\hat{c}_j$ axis in the body frame coordinates and is the line from the samara's center of mass $M_1$ to the marker located in the positive $\hat{f}_y$ direction $M_2$. The remaining basis requires an intermediate vector from which to compute a cross product defining the $\hat{c}_k$ axis as follows:

$$\delta_{1,2} = M_1 - M_2 \tag{15}$$

$$\delta_{1,3} = M_1 - M_3 \tag{16}$$

$$v = \frac{\delta_{1,3}}{\|\delta_{1,3}\|} \tag{17}$$

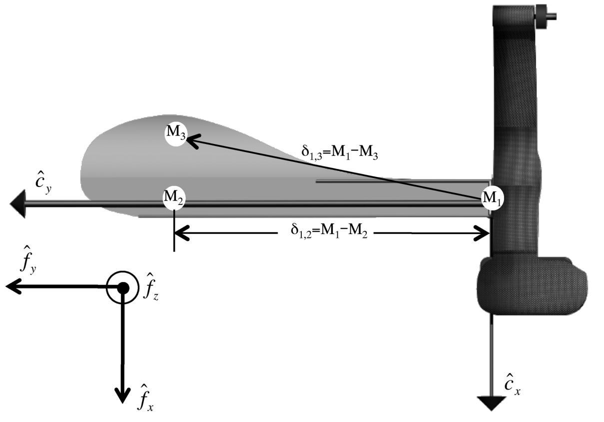

Fig. 6 Retroreflective marker placement.

A schematic detailing the construction of the vectors is shown in Fig. 6. The intermediate vector $\delta_{1,2}$ can be normalized, forming the $\hat{c}_i$ body frame axis. The vector $v$ is formed by normalizing $\delta_{1,3}$. This vector is then used to compute the body frame $\hat{c}_k$ axis. The final body axis is formed in the cross product of $\hat{c}_k$ and $\hat{c}_i$. This set forms the orthonormal basis that defines the orientation of the body with respect to the inertial frame:

$$\hat{c}_i = \frac{\delta_{1,2}}{\|\delta_{1,2}\|} = \alpha_{11} + \alpha_{21} + \alpha_{31} \tag{18}$$

$$\hat{c}_k = v \times \hat{c}_i = \alpha_{13} + \alpha_{23} + \alpha_{33} \tag{19}$$

$$\hat{c}_j = \hat{c}_k \times \hat{c}_i = \alpha_{12} + \alpha_{22} + \alpha_{32} \tag{20}$$

Once the 3-D marker position is obtained and the basis set of the samara body axes is computed, the Euler angles can be deduced from the basis $[\hat{c}_i, \hat{c}_j, \hat{c}_k]$. The Euler angles provide a nonunique set of rotations that can describe the samara's orientation. The angles are computed as follows:

$$\theta = \arcsin -\alpha_{13} \tag{21}$$

$$\psi = \arctan \frac{\alpha_{11}}{\alpha_{12}} \tag{22}$$

$$\phi = \arctan \frac{\alpha_{23}}{\alpha_{33}} \tag{23}$$

However, a singularity arises near $\pi/2$ and, to maintain continuity of signs between successive time steps near the singularity, it is necessary to set $\psi = 0$ and compute the final angle $\phi$ as

$$\phi = \arctan \frac{\alpha_{21}}{\alpha_{31}} \tag{24}$$

A central difference scheme is used to calculate the Euler angular rates [$\dot{\phi}$, $\dot{\theta}$, and $\dot{\psi}$].

### E. Attitude Representation

Attitude representation requires separate basis for the fixed inertial axes **F** and the body axes, which are fixed to the vehicle center of mass and aligned with the principal inertial axis **B**:

$$\mathbf{F} = [\hat{f}_x, \hat{f}_y, \hat{f}_z] \tag{25}$$

$$\mathbf{B} = [\hat{c}_i, \hat{c}_j, \hat{c}_k] \tag{26}$$

$$[\mathbf{r}]_B = R_1(\phi) \cdot R_2(\theta) \cdot R_3(\psi) \cdot [\mathbf{r}]_F \tag{27}$$

The transformation from the inertial frame to that of the body frame is described by three Euler angles. The order of rotation is as follows: a yaw rotation $\psi$ about the $\hat{f}_z$ axis followed by a pitch rotation $\theta$ about the new $\hat{f}_y$ axis and, lastly, a coning rotation $\phi$ about the new $\hat{f}_x$ axis. The transformation matrix can then be written as

$$R_{BF} = \begin{bmatrix} c\psi c\theta & s\psi c\theta & -s\theta \\ c\psi s\theta s\phi - s\psi c\phi & c\psi c\phi + s\psi s\theta s\phi & c\theta s\phi \\ s\psi s\phi + c\psi s\theta c\phi & s\psi s\theta c\phi - c\psi s\phi & c\theta c\phi \end{bmatrix} \tag{28}$$

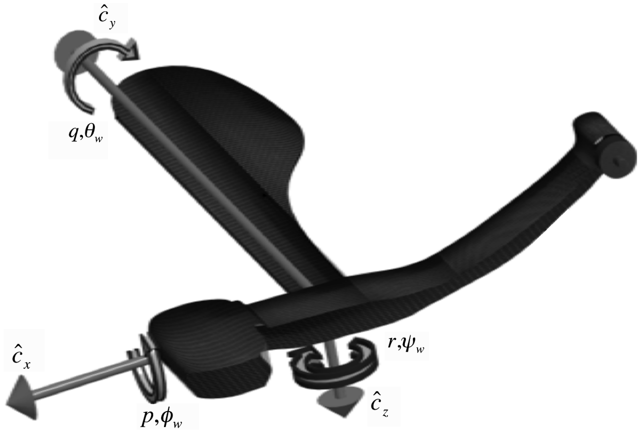

**Fig. 7 Robotic samara coordinate system.**

The notation is such that $s\theta = \sin\theta$ and $c\theta = \cos\theta$. This rotation sequence is standard for aircraft [10]. The Euler angular rates are defined in the inertial coordinate system (see Fig. 7). The angular rates in the inertial frame are finite rotations, which do not commute. It is thus necessary to define the body angular rates separately. The sum of the inner products of each of the inertial angular rates with the body axis of interest yields the body angular rates:

$$p = -\dot{\psi} \sin\theta + \dot{\phi} \tag{29}$$

$$q = \dot{\psi} \cos\theta \sin\phi + \dot{\theta} \cos\phi \tag{30}$$

$$r = \dot{\psi} \cos\theta \cos\phi - \dot{\theta} \sin\phi \tag{31}$$

### F. Kinematic Output

The Vicon-obtained estimates are exceptionally low-noise as compared with commercial-grade onboard attitude estimation sensors. The position noise variance was estimated by recording data while not moving the vehicle, shown in Table 3. The low-noise presence in the position estimate allows the inertial position to be numerically differentiated to yield inertial velocity estimates:

$$\{\dot{x}, \dot{y}, \dot{z}\}^T = \tfrac{\partial}{\partial t}\{x, y, z\}^T \tag{32}$$

The body-fixed velocities can be directly computed using the direction cosine matrix representation of the orientation estimate $R_{BF}$ and the inertial velocities as

$$\{u, v, w\}^T = R_{BF}\{\dot{x}, \dot{y}, \dot{z}\}^T \tag{33}$$

### G. Open-Loop Flight Test Data

The first step in system identification is to pilot the vehicle in a flight envelope where the dynamics of interest are thoroughly excited. The vehicle was piloted within the capture volume of the vision system while simultaneously collecting the inputs and vehicle kinematics. The pilot excited the vehicle over a wide range of frequency content to best determine the relationship between input and output. For proper system identification, it is important to collect flight data as open loop, as a closed-loop feedback system would alter

**Table 3 Measurement characteristics**

| Measurement | Symbol(s) | Source[a] | Resolution | Variance | Unit |
|---|---|---|---|---|---|
| Time | $t$ | VPS | $1.000 \times 10^{-3}$ | —— | s |
| Control input | $\theta_0$ | VPS | —— | $7.8000 \times 10^{-3}$ | norm |
| Position | $x, y, z$ | VPS | —— | $0.613 \times 10^{-3}$ | m |
| Orientation | $\phi, \theta, \psi$ | VPS | —— | $7.800 \times 10^{-3}$ | rad |
| Translational velocity | $u, v, w$ | VPS | —— | $0.251 \times 10^{-3}$ | m/s |
| Rotational velocity | $p, q, r$ | VPS | —— | $1.200 \times 10^{-3}$ | rad/s |

[a] VPS denotes visual positioning system.

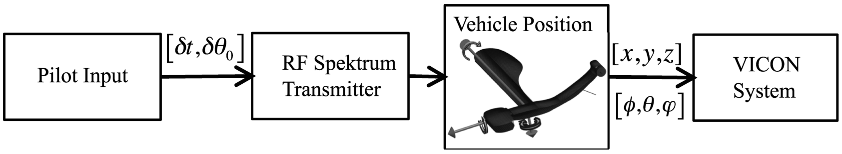

**Fig. 8 Open-loop control setup.**

the natural dynamics of the vehicle. The open-loop setup is shown in Fig. 8.

Typical portions from recorded open-loop data sets are shown in Fig. 9. The heave velocity $w$ is found by applying the central difference approximation to the vehicle vertical position data collected by the Vicon system. Figure 9 also compares the inputs given to the vehicle during one flight test, as calculated both onboard and offboard the robotic samara. Both onboard and offboard methods demonstrate similar pitch inputs, but the onboard measurements display more oscillations.

### H. Closed-Loop Flight Test Data

Implementation of closed-loop flight is enabled by an offboard feedback system. The ground control station setup is shown in Fig. 10. During closed-loop flight, the position and orientation of the robotic samara are tracked by the Vicon visual system, which sends the information to a LabVIEW controller program [11]. The LabVIEW program takes into account the vehicle's vertical position and heave velocity to create wing collective commands that are sent through a PIC-18F8722 microcontroller. The programmable interface microcontroller in turn sends the commands to the vehicle through a Spektrum transmitter.

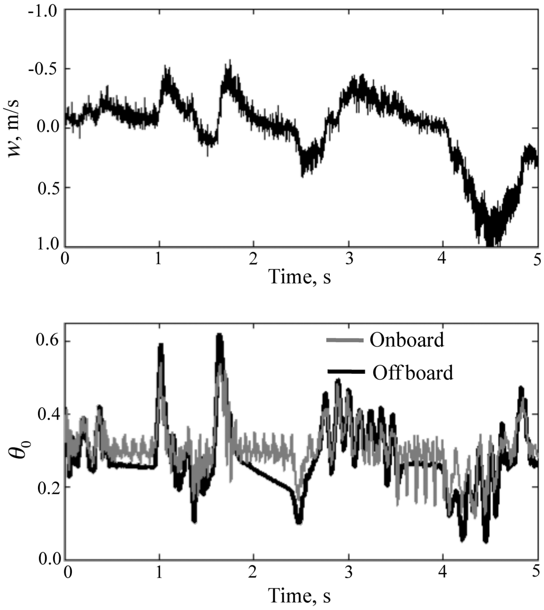

**Fig. 9 Flight data collected on samara I.**

## VI. Experimental Results

### A. System Identification Method

A beneficial step in the identification process is computing the coherence function. This step provides a measure of the extent to which an output is linearly related to the input over some frequency range [2]. The magnitude squared coherence is given by

$$\gamma_{xy}^2(\omega) \equiv \frac{|R_{xy}(\omega)|^2}{|R_{xx}(\omega)||R_{yy}(\omega)|} \tag{34}$$

An input/output pair with low coherence implies either the input has no effect on the output or the effect is nonlinear. However, an input/output pair with high coherence implies the relationship can be modeled well by a linear model, such as a transfer function or state-space model. Tischler and Remple [2] suggest a coherence of 0.6 or above for some useful frequency range is necessary for accurate transfer function identification.

The magnitude-squared coherence for the input/output relationship of samara I, using the onboard actuator system for input measurement, is shown in Fig. 11. It can be seen that the useful frequency for this input/output pair lies in the range of 0.3 to 10 Hz. The coherence and useful frequency range predicted by the onboard measured $\theta_0$ is equivalent to that of the offboard measurement (Fig. 11). The similarity of the two predictions validates the hypothesis that offboard measurements of $\theta_0$ are capable of capturing the physics relevant for system identification. The onboard measurement of $\theta_0$ for samara II demonstrates some high frequency behavior above 55 rad/s and may be a result of the aeroelasticity of the wing in flight (Fig. 11). Samara I does exhibit lower correlation than samara II below 5 Hz, most likely due to less excitation of samara I in that frequency range as compared with samara II. Despite the lower frequency content observed in the flight test of samara I, all three coherence plots demonstrate similar ranges for strong relationships between input and output.

### B. Open-Loop Control

The transfer function of the pitch-input-to-heave dynamics was modeled as a first-order continuous-time process model:

$$G_p(s) = \frac{K}{s - T_{pl}} = \frac{W(s)}{\Theta(s)} \tag{35}$$

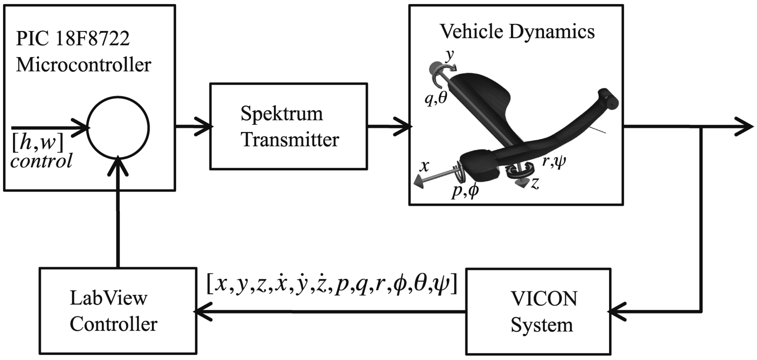

**Fig. 10 Ground control station (closed loop).**

**Table 4 Identified robotic samara parameters**

| | Samara I | Samara I | Samara II |
|---|---|---|---|
| $\theta_0$ | Offboard | Onboard | Onboard |
| $K$ | $-13.643$ | $-24.689$ | $-21.44$ |
| $T_{pl}$ | $-4.864$ | $-3.814$ | $-1.690$ |

Given a flight data set with sufficient coherence, as seen in Fig. 11, the MATLAB® system identification toolbox [12] can be used to compute frequency response-based system identification. The input and output data are imported to the system identification graphical user interface GUI where it is filtered to 100 rad/s using a fifth-order Butterworth filter.

Table 4 shows the values identified for the robotic samara for the collective-to-heave velocity transfer function using data from both methods of measuring pitch input. In comparing the two methods of identification, it is important to note that both methods identify $K$ and $T_{pl}$ to be on the same order of magnitude, proving both methods have similar capabilities in capturing the input/output relationship. The transfer functions of the computed models are plotted in Figs. 11 and 12.

### C. Error Analysis

A state-space model was created allowing for error estimation, using the CR bounds, and is represented as

$$\dot{X} = AX + BU \tag{36}$$

$$Y = CX \tag{37}$$

The state-space model for this identification reduces to

$$\dot{w} = Z_w w - Z_{\theta_0 \theta_0} \tag{38}$$

The CR bounds are theoretical minimum limits for the expected standard deviation in the parameter estimates, which would be obtained from several experiments [2]. Tischler and Remple suggest the following conditions represent the most valid parameter estimates: CR $\leq 20\%$ and $\bar{I} \leq 10\%$. The CR and $\bar{I}$ percentages were found using the Comprehensive Identification of Frequency Responses software (CIFER) [13]. Table 5 shows the parameter estimates and associated error bounds of the identified state-space model and demonstrates the validity of the identified parameter estimates, as all parameters meet the conditions specified.

The model computed from both on/offboard measurement of the collective angle input is capable of capturing most of the low-frequency inputs but can be seen to average higher-frequency excitation. The model computed from the offboard measurement of the collective angle input performs well at the lower frequencies but tends to average the higher-frequency excitation. The model exhibits more overshoot than that of the model derived from onboard measurements. The small differences in the performance of the two

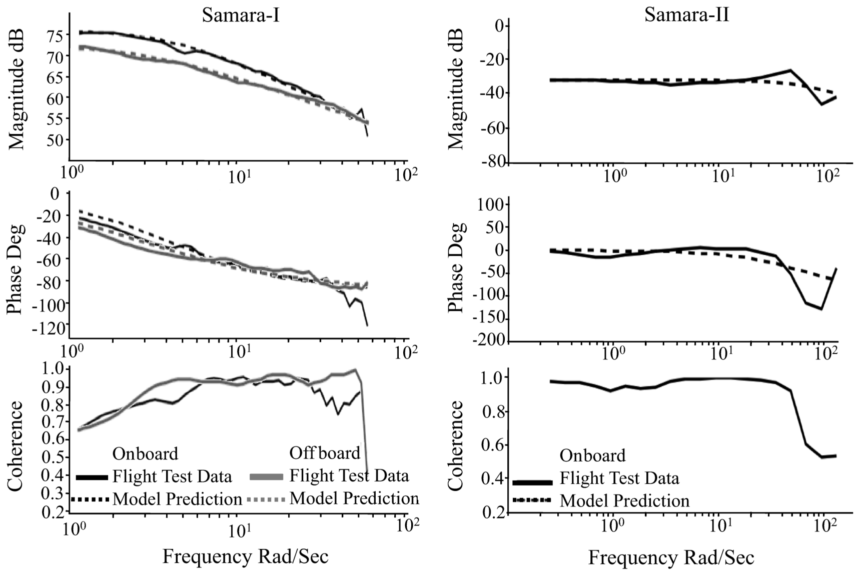

**Fig. 11 Robotic samaras I and II Identified model Bode diagram with corresponding data coherence, for onboard and offboard data collection and transfer function $G(s) = K/(s - T_{pl})$.**

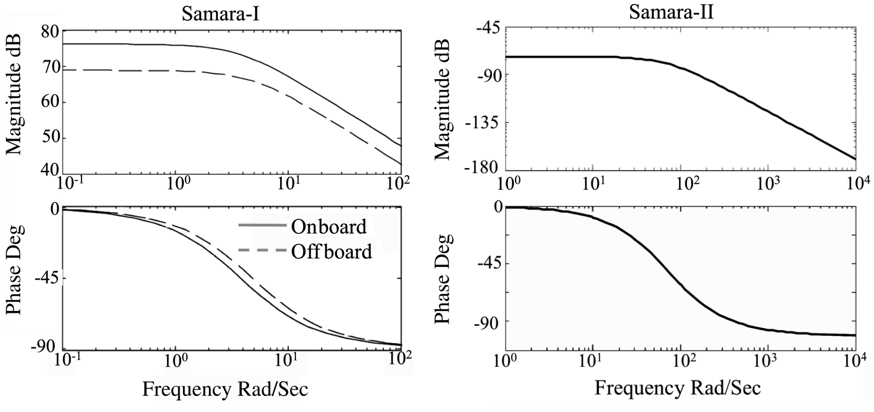

**Fig. 12 Robotic samaras I and II identified model Bode diagram, for onboard and offboard data collection and transfer function $\dot{w} = Z_w w - Z_{\theta_0 \theta_0}$.**

**Table 5 Robotic samara-identified parameter with CR error estimates**

| | Term | Value | CR, % | $\bar{I}$, % |
|---|---|---|---|---|
| Onboard samara I | $Z_w$ | −6.382 | 10.04 | 4.231 |
| | $Z_{\theta_0}$ | −15.880 | 4.733 | 1.994 |
| Offboard samara I | $Z_w$ | −4.303 | 9.413 | 3.808 |
| | $Z_{\theta_0}$ | −28.130 | 5.022 | 2.032 |
| Onboard samara II | $Z_w$ | −20.640 | 13.670 | 2.064 |
| | $Z_{\theta_0}$ | −1.501 | 12.840 | 1.939 |

methods of input measurement validate the ground-based input observation method. A comparison of the poles identified by MATLAB and CIFER is displayed in Fig. 13. The control derivative is a negative number as an increase in collective pitch $\theta_0$ and results in an increase in rotor thrust.

### D. Heave Dynamics

The heave dynamics of the robotic samara in hover are described by

$$\dot{w} - Z_w w = 0 \tag{39}$$

which has the analytical solution

$$w(t) = w_0 e^{Z_w t} \tag{40}$$

Because the stability derivative $Z_w$ is negative, the motion following a heave perturbation is a stable subsidence, as shown in Fig. 14. For example, a positive heave perturbation will generate an upflow through the robotic samara rotor disk and increase thrust, which acts in the negative direction of the $\hat{c}_z$-body axis. This also implies that, in hover, the robotic samara will have a real negative pole, as shown in Fig. 13. It is also possible to obtain the expression for altitude loss due to a velocity perturbation $w_0$. For a robotic samara in hover, $w = \dot{z}$ and

$$z(t) = \int_0^t w\,\mathrm{d}t + z_0 = w_0 \int_0^t e^{Z_w t}\,\mathrm{d}t + z_0 \tag{41}$$

where $z_0$ is the initial altitude. Integrating from $\{0, t\}$ yields

$$z(t) = z_0 - \frac{w_0}{Z_w}[1 - e^{Z_w t}] \tag{42}$$

from which the asymptotic value of altitude loss is

$$\lim_{t\to\infty} \Delta z = -\frac{w_0}{Z_w} \tag{43}$$

The robotic samara altitude change in response to a perturbation of heave velocity is shown in Fig. 14.

### E. Heave Response to Pilot Input

Consider a step input of collective pitch $\theta_0 = 0.4$. After a change of variables, the heave dynamic equation can be written as

$$\dot{w}_1 - Z_w w_1 = 0 \tag{44}$$

where

$$w_1(t) = w(t) + \frac{Z_{\theta_0}}{Z_w}\theta_0; \qquad \dot{w}_1 = \dot{w} \tag{45}$$

The analytic solution of the first-order differential equation is

$$w_1(t) = w_{1_0} e^{Z_w t} \tag{46}$$

with

$$w_{1_0} = \{w + \frac{Z_{\theta_0}}{Z_w}\theta_0\}_{t=0^+}$$

For the robotic samara in a steady hover, $w = 0$, which reduces the solution of $w_1(t)$ to

$$w_1(t) = \frac{Z_{\theta_0}}{Z_w}\theta_0 e^{Z_w t} \tag{47}$$

Thus, the heave velocity response to a step input of collective pitch reduces to

$$w(t) = -\frac{Z_{\theta_0}}{Z_w}\theta_0(1 - e^{Z_w t}) \tag{48}$$

An example of the first-order character of the vertical speed response to a step input of collective pitch is shown in Fig. 15. This is a basic characteristic of the behavior of a robotic samara and is clearly

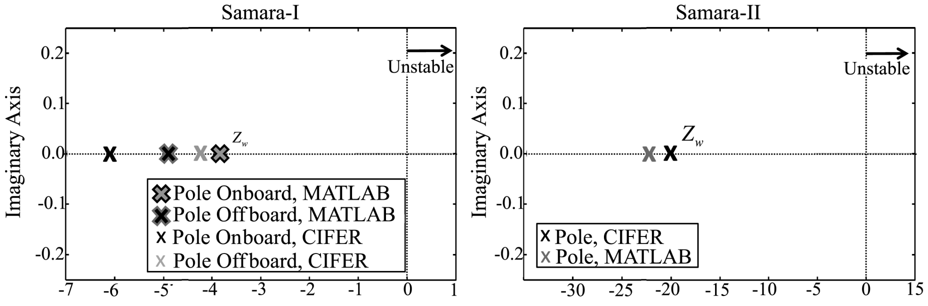

**Fig. 13 Real negative heave pole for robotic samaras I and II.**

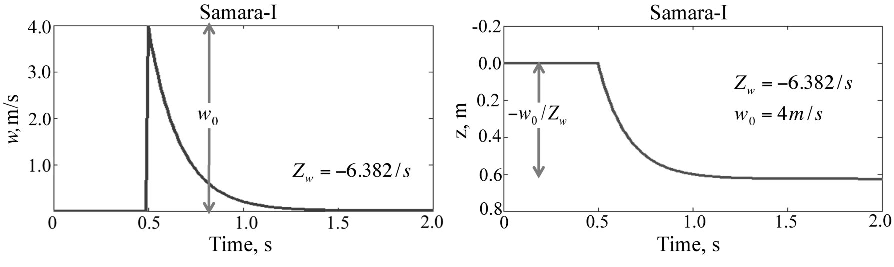

**Fig. 14 Motion following a perturbation $w_0$ of heave velocity.**

identifiable in results obtained from mathematical models and flight tests.

### F. Closed-Loop Feedback Control

Feedback control is used to correct for perturbations in the system in order to keep the vehicle at a reference condition. The structure of the closed-loop system is depicted in Fig. 16. Precise attitude data are collected by the Vicon motion capture system. The commanded altitude of the samara is maintained by feeding back the error in position to a control loop that contains the system and actuator dynamics. The closed-loop system attempts to compensate for errors between the actual and reference height of the samara by measuring the output response, feeding the measurement back and comparing it to the reference value at the summing junction. If there is a difference between the output and the reference, the system drives the plant to correct for the error [14].

A proportional plus derivative plus integral (PID) controller was chosen for feedback control of the robotic samara. A PID controller is given by the equation,

$$K(s) = K_p + K_d s + \frac{K_i}{s} \tag{49}$$

A PID controller feeds the error plus the derivative of the error forward to the plant. The proportional gain provides the necessary stiffness to allow the vehicle to approach the reference height. The proportional gain improves the steady-state error but causes overshoot in the transient response, whereas the derivative gain improves transient response. The integral term is proportional to both the magnitude and duration of the error in position, with the effect of eliminating the steady-state error. Using the ground control station setup described in Fig. 10 for closed-loop feedback control, several gain combinations were tested in order to find the PID gains, providing the best transient response to a change in reference height. Figure 17 depicts a representative data set of a flight test with the implementation of the PID controller, using the gains in Table 6, demonstrating that the actual height closely matches the reference height.

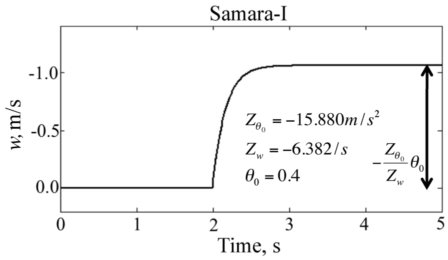

**Fig. 15 Robotic samara heave response to a step input of collective pitch.**

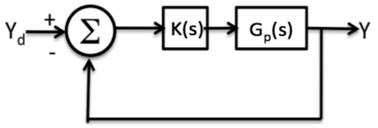

**Fig. 16 Prototypical feedback control loop.**

**Table 6 PID gains for feedback control**

| Gain | Samara I | Samara II |
|---|---|---|
| $K_p$ | 0.211 | 0.344 |
| $K_d$ | 0.889 | 0.133 |
| $K_i$ | 0.028 | 0.020 |

The dashed line in Fig. 17 is the altitude specified by the ground station. The solid line is the vehicle's vertical flight path. The change in altitude specified for ascent and descent are the same and, for a linear controller, the initial change in collective input is also the same. However, the resulting heave velocity in ascent is half the value observed in descent for both the samara I and samara II. The characteristic overdamping in climb and underdamping in descent of samaras I and II are the result of gravity's effect on the vehicle. In climb, the input wing force is greater than and opposite the force of gravity and, in descent, the same input wing force is in the direction of the force of gravity, resulting in a greater acceleration. The settling time $T_s$ of the samara I for a climbing maneuver is 1.03 s with no overshoot. A descending maneuver settles to 90% of the final value within 1.45 s, with an overshoot of 22%. The smaller samara II reached 90% of its final value in 1.7 s, with an overshoot of 60% for a descent maneuver. The settling time for a climbing maneuver is 0.7 s, with a 4% overshoot. It can be seen that the forces induced on the body from a change in collective pitch are substantial when compared with the inertia of the vehicle, as increases in heave velocity are quickly damped after excitation.

## VII. Conclusions

This work presented the identification of a linear model, describing the heave dynamics of two robotic samara vehicles for use in future control and state estimation. A visual positioning system was used to collect flight data while the vehicles were piloted in an indoor laboratory. Eigenvalues of the heave dynamic model were estimated by two system identification packages. The identified parameters were used in simulating the vehicles response to heave and collective input perturbations, as well as in the development of a PID controller. Closed-loop implementation of the derived controller was demonstrated using the visual tracking system for position and velocity feedback. The characteristically underdamped response to a descent maneuver was found, which differs from the critically damped response to an ascent maneuver.

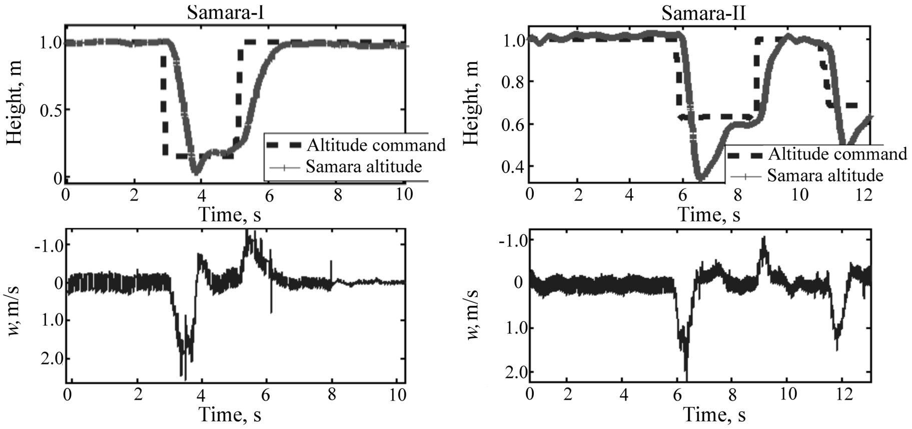

**Fig. 17 Implementation of PID control.**

## Acknowledgments

Thanks to the faculty and staff of the University of Maryland for so graciously providing the facilities for these experiments. Thanks to Joe Conroy for his expertise on system identification and for providing the electronics and feedback control interface. Thanks to Steven Gerardi for his assistance in the experimentation phase of the work.

## References

[1] Conroy, J., Humbert, J., and Pines, D., "System Identification of a Rotary Wing Micro Air Vehicle," *Journal of the American Helicopter Society* (submitted for publication).

[2] Tischler, M., and Remple, R., *Aircraft and Rotorcraft System Identification: Engineering Methods with Flight Test Examples*, AIAA, Reston, VA, 2006.

[3] Mettler, B., Tischler, M. B., Kanade, T., "System Identification Modeling of a Small-Scale Unmanned Rotorcraft for Control Design," *Journal of the American Helicopter Society*, Vol. 47, No. 1, Jan. 2002, pp. 50–63.
doi:10.4050/JAHS.47.50

[4] Graham, F., *Monocopters*, Perigee Press, East Liverpool, OH, 1999.

[5] Jameson, S., Allen, N., and Youngren, H., "SAMARAI Nano Air Vehicle: A Revolution in Flight," *AUVSI Unmanned Systems North America Conference Proceedings*, Washington, D.C., Aug. 2007.

[6] Ulrich, E., and Pines, D., "Planform Geometric Variation, and its Effect on the Autorotation Efficiency of Mechanical Samara," *AHS 64th Annual Forum*, American Helicopter Society, Alexandria, VA, 2008, pp. 1138–1149.

[7] Ulrich, E., and Pines, D., "Effects of Planform Geometry on Mechanical Samara Autorotation Efficiency and Rotational Dynamics," *Journal of the American Helicopter Society* (submitted for publication).

[8] Pines, D., and Bohorquez, F., "Challenges Facing Future Micro-Air-Vehicle Development," *Journal of Aircraft*, Vol. 43, No. 2, 2006, pp. 290–305.
doi:10.2514/1.4922

[9] Baruh, H., *Analytical Dynamics*, McGraw–Hill, New York, 1999.

[10] Stevens, B. L., and Lewis, F. L., *Aircraft Control and Simulation*, Wiley, Hoboken, NJ, 2003.

[11] LabVIEW User Manual, Ver. 8.2National Instruments, Austin, TX, 2008, http://www.ni.com/pdf/manuals/371361b.zip [retrieved Aug. 2006].

[12] System Identification Toolbox, Software Package, Ver. 7.0, The MathWorks, Natick, MA, 2008.

[13] Comprehensive Identification of Frequency Responses (CIFER), Software Package, U.S. Army Aeroflightdynamics Directorate, 2008.

[14] Nise, N., *Control Systems Engineering*, 4th ed., Wiley, Hoboken, NJ, 2004.